IEICE TRANS. ELECTRON., VOL.E84–C, NO.12 DECEMBER 2001



PAPER Special Issue on New Technologies in Signal Processing for Electromagnetic-wave Sensing and Imaging

# Polarimetric SAR Interferometry for Forest Analysis Based on the ESPRIT Algorithm

Hiroyoshi YAMADA[†a)], Yoshio YAMAGUCHI[†], *Regular Members*, Yunjin KIM[††], Ernesto RODRIGUEZ[††], *Nonmembers*, *and* Wolfgang-Martin BOERNER[†††], *Regular Member*

**SUMMARY** Synthetic aperture radar interferometry have been established in the past two decades, and used extensively for many applications including topographic mapping of terrain and surface deformation. Vegetation analysis is also a growing area of its application. In this paper, we propose an polarimetric SAR interferometry technique for interferometric phase extraction of each local scatterer. The estimated position of local scattering centers has an important information for effective tree height estimation of forest. The proposed method formulated for local scattering center extraction is based on the ESPRIT algorithm which is known for high-resolution capability of closely located incident waves. The method shows high-resolution performance when local scattered waves are uncorrelated and have different polarization characteristics. Using the method, the number of dominant local scattering centers and interferometric phases in each image pixel can be estimated directly. Validity of the algorithm is demonstrated by using examples derived from SIR-C data.

***key words:*** *synthetic aperture radar, interferometry, polarimetry, vegetation, ESPRIT algorithm*

## 1. Introduction

The precise three-dimensional measurement of terrain surface and deformation observations can be realized by the establishment of air- and space-borne interferometric SAR techniques [1]. In these radar observations, various microwave frequency bands (X, C, L, P-Band) are employed. When we observe terrain using C or L-Band data, it is known that back-scattered waves due to the volume scattering components from the forest canopy, in addition to ground reflections, are included in the observed radar signals so that the interferometric coherence decreases [2]–[4]. This means that the observed signals include information of both the ground surface and the forest canopy.

Recently, many research studies have been proposed for biomass estimation using the interferometric approach. The back-scattering waves resulting from the forest region can be expressed in terms of several parameters of ground and canopy scattering mechanisms. Therefore, multi-baseline and/or polarimetric techniques are required to acquire sufficient information for the parameter inversion [5]–[8].

In this paper, we focus on the polarimetric technique. Polarization is sensitive to the shape, orientation, textural fine structure, and dielectric constant variations inside a canopy volume. Therefore, polarimetry is one of the promising techniques for forest -versus- ground scattering estimation [9]. Cloude and Papathannassou utilized these properties and realized '*Polarimetric SAR Interferometry*' based on the coherence optimization [7], [10]. In addition, a parameter inversion technique, using the optimization, was proposed by them [11]. This technique is very attractive. However, this particular multiple inversion approach [9] requires multi-parameter least-square estimation whose complexity is high, and often becomes ill-conditioned.

In this paper, we propose an alternate '*Polarimetric SAR Interferometry*' technique based on the ESPRIT (*Estimation of Signal Parameters via Rotational Invariance Techniques*) algorithm [12]. The ESPRIT algorithm is often employed for '*Direction-Of-Arrival (DOA) Estimation*' for antenna arrays. We show, in this paper, that interferometric phases of ground and canopy can be directly resolved by this algorithm. When these phases are estimated, the derivation of the remaining parameters of the forest canopy becomes less complicated.

## 2. Canopy Scattering Model

For forest observations, the backscattered waves can be considered as the sum of the following components: (I) random volume backscatter from a non-penetrable layer of discrete scatterers in/on the canopy; (II) single scattering from tree trunks; (III) surface scattering after propagation through a random medium; (IV) low-order multiple scattering between the surface and trunks; (V) and back scattering from a rough surface [13] as illustrated in Fig. 1(a). These components can be classified into two groups: the first one corresponds to the waves whose local scattering center is located in the forest canopy (I, II); and the other corresponds to the waves whose local scattering center is located

Manuscript received March 29, 2001.
Manuscript revised June 29, 2001.

[†]The authors are with the Department of Information Engineering, Niigata University, Niigata-shi, 950-2181 Japan.
[††]The authors are with Jet Propulsion Laboratory, California Institute of Technology, Pasadena, CA 91109-8099, USA.
[†††]The author is with the University of Illinois at Chicago, Chicago, IL 60607-7018, USA.
a) E-mail: yamada@ie.niigata-u.ac.jp

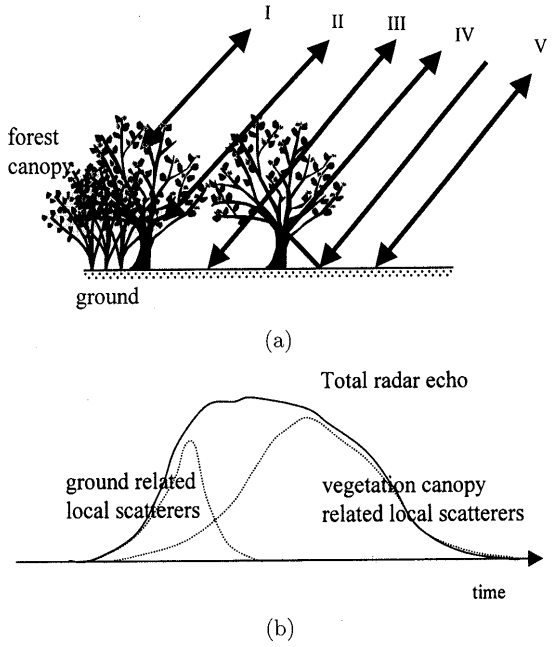


**Fig. 1** Waves scattered from vegetated region in radar remote sensing for the L-Band. (a) Local scattering mechanism of vegetated region, (b) Returned pulse shape model.

approximately on the ground (III, IV, V). Therefore, the distribution of the effective scattering coefficient across the forested terrain can be approximately modeled in terms of these two components [3] as depicted in Fig. 1(b). These two scattered waves are caused by different scattering mechanism, therefore their polarization state will be different [13]. Qualitative analysis can be found in [9]. Since the observed signals can be modeled in terms of these two components possessing different local scattering centers, the scattering centers estimated by the interferometric phase are located between the upper canopy layer and the ground; and the interferometric coherence decreases because the components, in Fig. 1(a), are not fully correlated, in general. Assuming that the canopy layer can be modeled as a random medium, the complex coherence of the random volume plus ground scattering can be formulated [8], [9], [11] by

$$\gamma = e^{j\phi_0}\frac{\gamma_T\gamma_V + m(\boldsymbol{\omega})}{1+m(\boldsymbol{\omega})}, \tag{1}$$

where

- $\phi_0$ : underlying topographic phase,
- $\gamma_V$ : complex coherence due to volume scattering,
- $m(\boldsymbol{\omega})$: ratio of ground to volume scattering amplitudes,
- $\gamma_T$ : temporal coherence,
- $\boldsymbol{\omega}$ : a unitary scattering mechanism polarization dependency.

Assuming that the temporal effects are negligibly small ($\gamma_T = 1$), the number of unknowns in Eq. (1) becomes 6 ($m_i$ $(i = 1, 2, 3)$ independent polarization mechanisms, and $|\gamma_V|$, $\phi_0$, $\phi_V$). In fully polarimetric observations, we obtain three independent complex coherence expressions (e.g., HH, HV (= VH), and VV in the HV-basis. or, three optimized coherence expressions [10]). By Defining these three coherence expressions as $\gamma_1, \gamma_2$, and $\gamma_3$, the equation to be solved, can be written as

$$\begin{bmatrix} e^{j\phi_0} \\ e^{j\phi_V} \\ |\gamma_V| \\ m_1 \\ m_2 \\ m_3 \end{bmatrix} = \mathcal{M}^{-1}\begin{bmatrix} \gamma_1 \\ \gamma_2 \\ \gamma_3 \end{bmatrix}, \tag{2}$$

where $\phi_V$ is the phase of $\gamma_V$ and the operator $\mathcal{M}$ represents the scattering model. When these parameters can be estimated, the real effective tree height, etc., can be recovered and calculated.

Now, to consider the model from a different point of view, we rewrite Eq. (1) by

$$\begin{aligned}\gamma &= \frac{m(\boldsymbol{\omega})}{1+m(\boldsymbol{\omega})}e^{j\phi_0} + \frac{\gamma_T|\gamma_V|}{1+m(\boldsymbol{\omega})}e^{j(\phi_0+\phi_V)} \\ &= \sigma_1 e^{j\phi_1} + \sigma_2 e^{j\phi_2},\end{aligned} \tag{3a}$$

where,

$$\sigma_1 = \frac{m(\boldsymbol{\omega})}{1+m(\boldsymbol{\omega})}, \qquad \sigma_2 = \frac{\gamma_T|\gamma_V|}{1+m(\boldsymbol{\omega})}, \tag{3b}$$

$$\phi_1 = \phi_0, \qquad \phi_2 = \phi_0 + \phi_V. \tag{3c}$$

Clearly, this equation shows that the total coherence can be expressed by the sum of two components; one component having its scattering center on the ground ($\sigma_1 e^{j\phi_1}$), and the other in the canopy ($\sigma_2 e^{j\phi_2}$), which also coincide with the model shown in Fig. 1.

## 3. Problem Formulation

The dominant scattering components in the forest region, observed at each radar site, are considered to consist at least of two components; however, we generalize it to be $d$ independent components. In this case, using the geometry of Fig. 2, the observed signals in '*orbit-1(master orbit)*' and in '*orbit-2 (slave orbit)*' may be written as

$$E_1^{(kl)} = \sum_{i=1}^{d}\sigma_i s_i^{(kl)} e^{j\frac{4\pi}{\lambda}\rho} + n_1^{(kl)}, \tag{4a}$$

$$E_2^{(kl)} = \sum_{i=1}^{d}\sigma_i' {s_i}'^{(kl)} e^{j\frac{4\pi}{\lambda}(\rho+\Delta\rho_i)} + n_2^{(kl)}, \tag{4b}$$

where $k$ and $l$ denote polarization combinations (e.g., HH, HV, VH, VV); $s_i^{(kl)}$ and ${s_i}'^{(kl)}$ denote the polarization state of the $i$-th local scatterer in the $kl$ polarization observed at the master and slave orbital receivers,

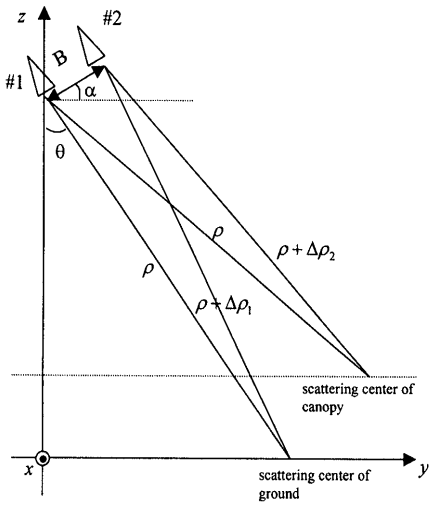


**Fig. 2** Interferometric SAR geometry.

respectively. These polarization states are assumed to be normalized with respect to the power of each local scatterer; $\sigma_i(\sigma_i')$ denotes the power of the $i$-th local scatterer observed at the master (slave) orbit; $\rho$ is the slant-range distance from the master orbit to the range-bin; $\Delta\rho_i$ in Eq. (4b) denotes the slant-range difference of the $i$-th scatterer at the slave orbit; and $n_1^{(kl)}$ and $n_2^{(kl)}$ denote the additive Gaussian noise in the $kl$ channel at the master and slave receivers, respectively. Although repeat-pass measurements are assumed for the above formulation, a similar formulation is also applicable for single-pass measurements. In the following formulations, we use the {HV}-polarization basis of 4 channels (HH, HV, VH, VV). Since HV$\simeq$ VH, the formulation for 3 channel data (HH, HV, VV) is essentially the same. In addition, the other polarization bases data, obtained from {HV}-basis measurements, are also applicable, which includes the Pauli representation [13].

Using matrix and vector expressions, Eqs. (4a) and (4b) can be written as

$$\begin{aligned}\boldsymbol{E}_1 &= \left[E_1^{(HH)}, E_1^{(HV)}, E_1^{(VH)}, E_1^{(VV)}\right]^T \\ &= \boldsymbol{S}\boldsymbol{\sigma} + \boldsymbol{n}_1, \qquad (5a)\\ \boldsymbol{E}_2 &= \left[E_2^{(HH)}, E_2^{(HV)}, E_2^{(VH)}, E_2^{(VV)}\right]^T \\ &= \boldsymbol{S}'\boldsymbol{\sigma}' + \boldsymbol{n}_2, \qquad (5b)\\ \boldsymbol{S} &= [\boldsymbol{s}_1, \boldsymbol{s}_2, \cdots, \boldsymbol{s}_d] \\ &= \begin{bmatrix} s_1^{(HH)} & \cdots & s_d^{(HH)} \\ s_1^{(HV)} & \cdots & s_d^{(HV)} \\ \vdots & & \vdots \\ s_1^{(VV)} & \cdots & s_d^{(VV)} \end{bmatrix} \qquad (5c)\end{aligned}$$

$$\begin{aligned}\boldsymbol{S}' &= [\boldsymbol{s}_1', \boldsymbol{s}_2', \cdots, \boldsymbol{s}_d'] \\ &= \begin{bmatrix} s_1'^{(HH)} & \cdots & s_d'^{(HH)} \\ s_1'^{(HV)} & \cdots & s_d'^{(HV)} \\ \vdots & & \vdots \\ s_1'^{(VV)} & \cdots & s_d'^{(VV)} \end{bmatrix} \qquad (5d)\\ \boldsymbol{\sigma} &= \left[\sigma_1 e^{j\frac{4\pi}{\lambda}\rho}, \cdots, \sigma_d e^{j\frac{4\pi}{\lambda}\rho}\right] \qquad (5e)\\ \boldsymbol{\sigma}' &= \left[\sigma_1' e^{j\frac{4\pi}{\lambda}(\rho+\Delta\rho_1)}, \cdots, \sigma_d' e^{j\frac{4\pi}{\lambda}(\rho+\Delta\rho_d)}\right] \qquad (5f)\\ \boldsymbol{n}_j &= \left[n_j^{(HH)}, n_j^{(HV)}, n_j^{(VH)}, n_j^{(VV)}\right]^T, j = 1, 2 \qquad (5g)\end{aligned}$$

where $T$ denotes transpose. Since the targets are located in the far-field region of the radar, and the look-angles at both orbits almost coincide, the polarization state of each local scatterer in both channels are assumed to be almost identical, or

$$s_i^{(kl)} \simeq s_i'^{(kl)}, \qquad \sigma_i \simeq \sigma_i'. \qquad (6)$$

Applying Eq. (6), Eq. (4b) can be simplified as follows:

$$\begin{aligned}\boldsymbol{E}_2 &= \boldsymbol{S}'\boldsymbol{\sigma}' + \boldsymbol{n}_2 \\ &\simeq \boldsymbol{S}\boldsymbol{D}\boldsymbol{\sigma} + \boldsymbol{n}_2, \qquad (7a)\\ \boldsymbol{D} &= diag\left\{e^{j\phi_1}, e^{j\phi_2}, \cdots, e^{j\phi_d}\right\}, \qquad (7b)\\ \phi_i &= \frac{4\pi}{\lambda}\Delta\rho_i. \qquad (7c)\end{aligned}$$

The interferometric phase of each scatterer can be estimated by $\boldsymbol{D}$ from Eqs. (5a) and (7a). These equations have the same form as those in the ESPRIT algorithm [12].

Here, we summarize the assumptions for applying the ESPRIT processing to '*Polarimetric SAR Interferometry*' as follows:

**A1.** Additive noise can be modeled as white Gaussian noise, which is independent for each channel.
**A2.** The local scattered waves can be well approximated in terms of Eqs. (5a) and (7a). This means that each wave has a dominant scattering center.
**A3.** The polarization state of each wave is assumed to be almost equal in both orbital observations.
**A4.** The locally scattered waves are not fully correlated (nor coherent).
**A5.** The auto-correlation of each local scattering wave is high.
**A6.** For repeat-pass applications, the temporal decorrelation effect is negligibly small.

Above assumptions will be accepted in general. Validity of **A2** will be a key factor; however, the meaning of the assumptions made is essentially the same for those made in the modeling approach introduced by Cloude, as briefly reviewed in Sect. 2.

## 4. The ESPRIT Algorithm

In this section, we briefly summarize the procedure of

the ESPRIT algorithm. The algorithm shown here is known as the TLS (Total Least Square) ESPRIT algorithm [12], which is effective for noisy data-vectors.

In the TLS-ESPRIT algorithm, we define the overall data vector by Eqs. (5a) and (7a) as,

$$\begin{aligned}\boldsymbol{x} &= \begin{bmatrix} \boldsymbol{E}_1 \\ \boldsymbol{E}_2 \end{bmatrix} = \begin{bmatrix} \boldsymbol{S} \\ \boldsymbol{SD} \end{bmatrix} \boldsymbol{\sigma} + \begin{bmatrix} \boldsymbol{n}_1 \\ \boldsymbol{n}_2 \end{bmatrix} \\ &= \bar{\boldsymbol{S}}\boldsymbol{\sigma} + \bar{\boldsymbol{n}}. \end{aligned} \tag{8}$$

The vector $\boldsymbol{x}$ is a $2M$-dimensional vector for $M$ channel data sets (In Eqs. (5a) and (7a), we define $M = 4$.). The correlation matrix of $\boldsymbol{x}$ is defined as follows:

$$\boldsymbol{R}_{xx} = <\boldsymbol{x}\boldsymbol{x}^H> = \bar{\boldsymbol{S}}\boldsymbol{\Sigma}_S\bar{\boldsymbol{S}}^H + \sigma_N^2\boldsymbol{\Sigma}_N, \tag{9a}$$

$$\boldsymbol{\Sigma}_S = <\boldsymbol{\sigma}\boldsymbol{\sigma}^H>, \tag{9b}$$

$$\boldsymbol{\Sigma}_N = <\boldsymbol{n}\boldsymbol{n}^H>, \tag{9c}$$

where $<\cdot>$ denotes ensemble averaging, or interferometric multi-look processing in the small image-patch area; $H$ denotes complex conjugate and transpose; $\sigma_N^2$ is the average noise power; and the matrices, $\boldsymbol{\Sigma}_S$ and $\boldsymbol{\Sigma}_N$, denote correlation matrices of local scattering waves and noise, respectively. When the assumptions **A1** and **A4** hold, the ranks of the correlation matrices become:

$$rank(\boldsymbol{\Sigma}_S) = d, \qquad rank(\boldsymbol{\Sigma}_N) = 2M.$$

Furthermore, if we can add a new assumption **A7**:

**A7.** Polarization states of each locally scattered wave are linearly independent of each other, or

$$\boldsymbol{s}_i \neq k\boldsymbol{s}_j, \quad i \neq j, \quad k\text{: complex constant}, \tag{10}$$

then $rank(\bar{\boldsymbol{S}}) = d$, and the following rank condition can also be derived, where

$$rank(\bar{\boldsymbol{S}}\boldsymbol{\Sigma}_S\bar{\boldsymbol{S}}^H) = d.$$

Therefore, by the eigenanalysis of $\boldsymbol{R}_{xx}$[†]:

$$|\boldsymbol{R}_{xx} - \lambda\boldsymbol{\Sigma}_N| = 0, \tag{11}$$

we can derive the following properties.

**Property-1:** Defining the eigenvalues of $\boldsymbol{R}_{xx}$ as $\lambda_1, \lambda_2, \cdots, \lambda_{2M}$; their magnitude distribution can be expressed by

$$\lambda_1 \geq \cdots \geq \lambda_d > \lambda_{d+1} = \cdots = \lambda_{2M} (= \sigma_N^2.) \tag{12}$$

When $d < M$ holds, the $2M - d$ smallest eigenvalues appear, whose magnitude are equal to the noise power. The number of dominant eigenvalues is $d$. The number of local scatterers, $d$, can be estimated by this property.

The total backscattered power of each regional patch highly changes depending on the property of its scene (terrain surface structure). Therefore, normalized eigenvalues, $\bar{\lambda}_j$, are effective to detect changes of eigenvalue distributions for each patch, where

$$\bar{\lambda}_j = \frac{\lambda_j}{\sum_{i=1}^{2M}\lambda_i}, \qquad j = 1,\ 2,\ \cdots,\ 2M. \tag{13}$$

Note the difference (contrast) between $\lambda_d$ and $\lambda_{d+1}$ depends not only on the scattering power of the signals ($\sigma_j$) but also on the orthogonality of the polarization state vector of the scatterer ($\boldsymbol{s}_j$). When all of the $\boldsymbol{s}_j$s are orthogonal, the difference becomes maximum.

**Property-2:** The eigenvectors, $\boldsymbol{e}_1, \boldsymbol{e}_2, \cdots, \boldsymbol{e}_d$, that correspond to the dominant eigenvalues can be expressed as follows:

$$[\boldsymbol{e}_1, \boldsymbol{e}_2, \cdots, \boldsymbol{e}_d] = \begin{bmatrix} \boldsymbol{F}_1 \\ \boldsymbol{F}_2 \end{bmatrix} = \begin{bmatrix} \boldsymbol{ST} \\ \boldsymbol{SDT} \end{bmatrix}, \tag{14}$$

where $\boldsymbol{T}$ denotes a $d \times d$ non-singular matrix.

Estimation of $\boldsymbol{D}$ can be realized by *Property-2*. In case the matrices, $\boldsymbol{F}_1, \boldsymbol{F}_2$, are obtained from noisy measurements, then we implement the TLS-ESPRIT algorithm.

Next, we define a matrix $\boldsymbol{F}_{12}$:

$$\boldsymbol{F}_{12} = [\boldsymbol{F}_1, \boldsymbol{F}_2]. \tag{15}$$

Since the rank of the matrix $\boldsymbol{F}_{12}$ is $d$, there exists a unique $2d \times d$ matrix $\boldsymbol{G}$ having rank $d$ that holds for the following equation,

$$\begin{aligned}\boldsymbol{0} &= \boldsymbol{F}_{12}\boldsymbol{G} = \boldsymbol{F}_1\boldsymbol{G}_1 + \boldsymbol{F}_2\boldsymbol{G}_2 \\ &= \boldsymbol{ST}\boldsymbol{G}_1 + \boldsymbol{SDT}\boldsymbol{G}_2, \end{aligned} \tag{16a}$$

$$\boldsymbol{G} = \begin{bmatrix} \boldsymbol{G}_1 \\ \boldsymbol{G}_2 \end{bmatrix}. \tag{16b}$$

The matrix $\boldsymbol{G}$ can be constructed by the eigenvectors corresponding to zero eigenvalues of $\boldsymbol{F}_{12}^H\boldsymbol{F}_{12}$ since the columns of the matrix $\boldsymbol{G}$ span a null-space of $\boldsymbol{F}_{12}$.

Here, we define a matrix $\boldsymbol{\Psi}$ as

$$\boldsymbol{\Psi} = -\boldsymbol{G}_1\boldsymbol{G}_2^{-1}. \tag{17}$$

And by substituting Eq. (17) into Eq. (16a), we obtain

$$\boldsymbol{ST}\boldsymbol{\Psi} = \boldsymbol{SDT}. \tag{18}$$

Hence, $\boldsymbol{D}$ can be expressed by

$$\boldsymbol{D} = \boldsymbol{T}\boldsymbol{\Psi}\boldsymbol{T}^{-1}. \tag{19}$$

From these results, the next relevant property can be derived.

[†]Generally, $\boldsymbol{\Sigma}_N$ is often unknown. In such a case, it may be appropriate to set $\boldsymbol{\Sigma}_N = \boldsymbol{I}$ as an approximate estimation.

**Property-3:** (Complex) Eigenvalues of the matrix defined by Eq. (17),

$$\lambda'_1, \lambda'_2, \ldots, \lambda'_d, \tag{20}$$

correspond to the diagonal elements of $\boldsymbol{D}$. Then, the interferometric phase of each local scatterer, $\phi_i$, can be estimated by

$$\phi_i = arg(\lambda'_i). \tag{21}$$

Note that the magnitude of the $\lambda'_i$s is almost equal to 1 when all of the assumptions (**A1**–**A7**) hold as shown in Eq. (7b).

When interferometric phases are estimated, the effective height of the local scatterers in simple InSAR configuration can be calculated by

$$\theta_i = (\pi/2 - \theta + \alpha) - \sin^{-1}\left(\frac{\lambda\phi_i}{4\pi B}\right), \tag{22a}$$

$$h_{eff,i} = H - \rho\cos\theta_i. \tag{22b}$$

Detailed discussion for height estimation can be found in [14].

Equation (21) means that we can directly estimate interferometric phases of local scatterers, or those corresponding to the canopy layer and the ground. These phases are the $\phi_0$ and $\phi_V$ in Eq. (2); therefore, finding the solution for the remaining parameters (and also of the effective tree height) will become easier.

The filtering sequence of inappropriate regional patches, for example, can be summarized as follows:

$$\sum_{j=1}^{2M} \lambda_j > \xi_0, \tag{23a}$$

$$\bar{\lambda}_i < \xi_1 \quad \text{for } d > 1 \text{ region}, \tag{23b}$$

$$||\lambda'_i| - 1| < \xi_2, \tag{23c}$$

where the $\xi_i$s denote appropriate threshold values. Equation (23a) is used to exclude the low SNR (in total power) region, whose phases are affected by noise. When there exist several scattering components, $\bar{\lambda}_1$ becomes small, then we can detect such a regional patch by using Eq. (23b). In case the estimation of *Property-3* will hold, Eq. (23c) provides the validity condition for this assumption. It is one of the promising advantages of the ESPRIT algorithm that various conditions can be checked concurrently during data processing.

These threshold values will depend on radar parameters (ex. resolution) and land surface. When there are patches whose scattering is extremely small, $\xi_0$ can be easily determined to omit the patches. Model order algorithm such as AIC [15] and MDL [16] will helps to select suitable $\xi_1$ for ideal case. The suitable threshold values selection for the actual data, it will be better to do several trials with different threshold values. When we evaluate patches, which have only one dominant scattering center, as $d = 2$, phase differences of the extracted phase centers will be distributed randomly because one of the estimated scatterers is corresponding to noise. Therefore, histogram of the estimated phase difference will also help to select suitable threshold values in the trials.

## 5. Experimental Results

The used experimental polarimetric SAR image data takes are L-band scattering single-look complex (SLC) image pairs of the Tien-Shan flight-path collected with the SIR-C/X-SAR system on October 8 and 9, 1994 (SAR image data takes 122.20 & 154.20). The total power image of the analyzed 'Kudara Polygon' region are shown in Fig. 3. The extracted area for this experiment is 1000 pixels in range and 5000 pixels in azimuth (6.7 km × 25.2 km approximately). The forest area is located at upper left of the image. Furthermore, in the right part around the Selenga River, there are shrub-land areas. The area between the forest and the river are farmland mainly. The Tien-Shan SIR-C/X-SAR image data takes used here are identical to the SIR-C/X-SAR Tien-Shan flight-pass set for the Selenga River delta region (Kudara Test Site) used by Cloude and Papathanassiou [7] and by Stebler, Pasquali and Nüesch [17] for testing their own '*Polarimetric SAR Interferometry*' models.

The HH, HV, and VV ($M = 3$) data sets are used for the fully polarimetric analysis. Then the data vectors are defined by,

$$\boldsymbol{E}_i = \left[E_i^{(HH)}, E_i^{(HV)}, E_i^{(VV)}\right]^T, \qquad i = 1, 2.$$

Therefore, we obtain 6 eigenvalues at each image patch for *Property-1*. The coherence maps of the largest 3 normalized eigenvalues ($\bar{\lambda}_i, i = 1, 2, 3$) defined in (13) are shown in Figs. 4(a)–(c). Gray-scale shows magnitude of the normalized eigenvalues. Note that $\bar{\lambda}_2$ and $\bar{\lambda}_3$ are shown with range from 0 to 0.5 because of their small magnitude, whereas $\bar{\lambda}_1$ is shown with range from 0 to 1.0. Since the eigenvalues are normalized with respect to the total power, the distribution becomes

**Fig. 3** L-Band total power image of the test area (Tien-Shan flight-path).

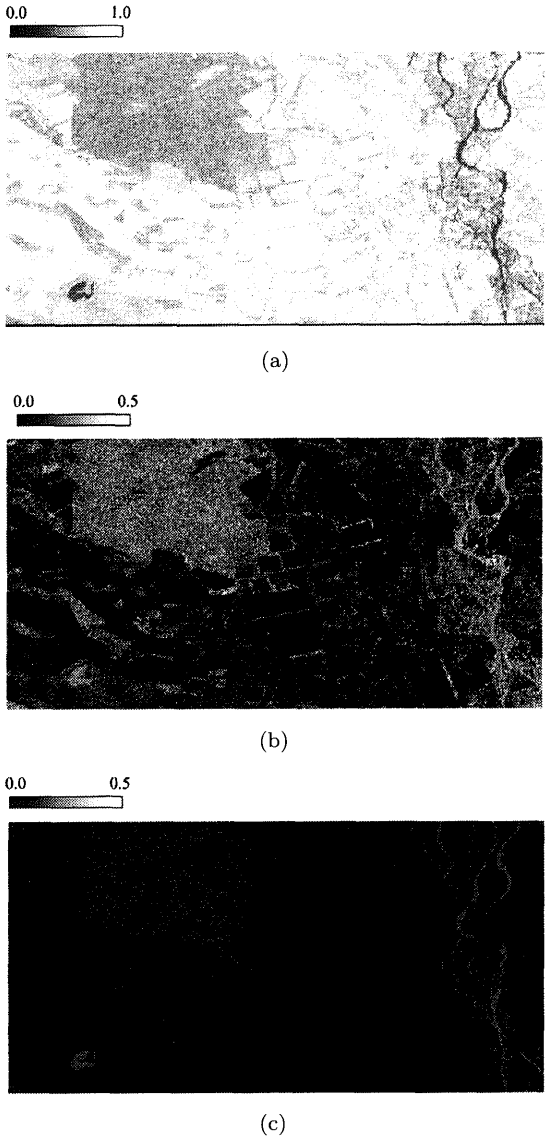


**Fig. 4** Normalized eigenvalue maps of the TLS-ESPRIT analysis. (a) $\bar{\lambda}_1$ map, (b) $\bar{\lambda}_2$ map, (c) $\bar{\lambda}_3$ map.

$\bar{\lambda}_1 \simeq 1, \bar{\lambda}_2 \simeq \bar{\lambda}_3 \simeq \sigma_N^2$ in the region where only one component exists. When there exist more than two components, $\bar{\lambda}_1$ decreases and $\bar{\lambda}_2$ increases. As can be seen in Fig. 4(a), the $\bar{\lambda}_1$s of the forest region are clearly small in comparison to the other regions. Therefore, it can be said that the forest regions are clearly discriminated from the other regions using the $\bar{\lambda}_1$ map. This property is useful for forest canopy detection. These eigenvalue maps also show the validity of Assumptions **A4** and **A5**.

Next, we estimate the interferometric phases of the forest region. In this analysis, two components can be detected because of $M = 3$. The threshold values in Eqs. (23a), (23b), and (23c) are selected, respectively, as follows:

$$\xi_0 = 0.15, \qquad \xi_1 = 0.8, \qquad \xi_2 = 0.25$$

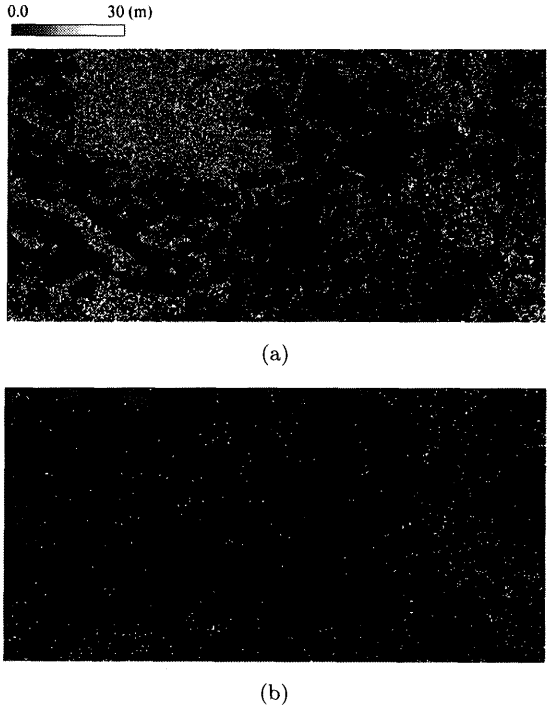


**Fig. 5** Maps of the estimated differential height and the spurious results distribution. (a) differential height map, (b) spurious results distribution.

Figure 5(a) shows the map of the differential height between scattering centers corresponding to $\phi_1$ and $\phi_2$, derived by using the technique in [14]†. In the figure, the regions for which above threshold conditions are violated, are plotted by "0." The patches in the large forest region at the upper left in the figure display the property that there exist two dominant components. There are several regions of extremely high height. Patches whose estimation height exceed 30 m are shown as white dots in Fig. 5(b). Since most of the spurious (incorrect) estimation results are distributed about the transition area between forest and (bare) surface, or sparse tree areas, these spurious (incorrect) results are caused by the inhomogeneity of the tree heights in the patch region (pixel cluster) used in the correlation matrix estimation of Eq. (9a). When we determine the patch regions carefully, we could decrease their improper contribution effectively.

Figure 6 shows the histogram of the differential height of Fig. 5(a). The peak of the differential height is located approximately at 10 m. Almost all results indicate a tree height of below 30 m. The real effective tree height will be slightly higher than these values, therefore, we can say that the estimated results are acceptable.

†Note that the estimated height shows *effective* tree height. Because height of the scattering center corresponding to the canopy depends on density of trees, shape of canopy and so forth.

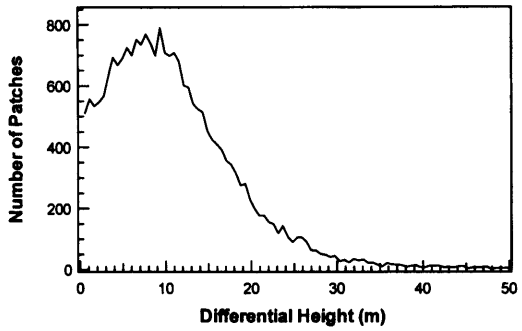


**Fig. 6** Histogram of the estimated differential height.

## 6. Conclusions

In this paper, we propose an alternate '*Polarimetric SAR Interferometry*' technique using the TLS-ESPRIT algorithm. The technique can work with both fully polarimetric image data takes; and it detects the local interferometric phase of the canopy and the ground separately. In addition, the validity of estimation results can be checked by the eigenvalue distributions. These properties are demonstrated for the SIR-C/X-SAR data sets for the Tien-Shan repeat-pass Kudara test-site within the Selenga River Delta.

To verify the estimation accuracy precisely, computer simulations are required. The performance of the algorithm for single-pass SAR image data take sets is another highly relevant project to be considered. In addition, relation between *effective* tree height estimated this method and *real* tree height to be considered in various forest types. The corresponding results will be reported in the near future.

### References

[1] P.A. Rosen, S. Hensley, I.R. Joughin, F.K. Li, S.N. Madsen, E. Rodriguez, and R.M. Goldstein, "Synthetic aperture radar interferometry," Proc. IEEE, vol.88, no.3, pp.333–382, March 2000.

[2] H.A. Zebker and J. Villasenor, "Decorrelation in interferometric radar echoes," IEEE Trans. Geosci. & Remote Sensing, vol.30, no.5, pp.950–959, Sept. 1992.

[3] J.O. Hagberg, L.M.H. Ulander, and J.I. Askne, "Repeat-pass SAR interferometry over forested terrain," IEEE Trans. Geosci. & Remote Sensing, vol.33, no.2, pp.331–340, March 1995.

[4] J.I. Askne, P.B.G. Dammert, L.M.H. Ulander, and G. Smith, "C-band repeat-pass interferometric SAR observations of the forest," IEEE Trans. Geosci. & Remote Sensing, vol.35, no.1, pp.25–35, Jan. 1997.

[5] R.N. Treuhaft, S.N. Madsen, M. Moghaddam, and J.J. van Zyl, "Vegetation characteristics and underlying topography from interferometric radar," Radio Science, vol.31, no.6, pp.1449–1485, Nov.–Dec. 1996.

[6] R.N. Treuhaft and P.R. Siqueria, "Vertical structure of vegetated land surfaces from interferometric and polarimetric radar," Radio Science, vol.35, no.1, pp.141–177, Jan.–Feb. 2000.

[7] S.R. Cloude and K.P. Papathanassiou, "Polarimetric SAR interferometry," IEEE Trans. Geosci. & Remote Sensing, vol.36, no.5, pp.1551–1565, Sept. 1998.

[8] K.P. Papathanassiou, S.R. Cloude, A. Reigber, and W.M. Boerner, "Multi-baseline polarimetric SAR interferometry for vegetation parameter estimation," Proc. IGRASS 2000, VI, pp.24–28, July 2000.

[9] K.P. Papathanassiou, A. Reigber, and S.R. Cloude, "Vegetation and ground parameter estimation using polarimetric interferometry Part 1: The role of polarisation," Proc. ESA CEOS SAR Workshop, pp.26–29, Oct. 1999.

[10] S.R. Cloude and K.P. Papathanassiou, "Polarimetric optimisation in radar interferometry," Electron. Lett., vol.33, no.13, pp.1176–1178, June 1997.

[11] K.P. Papathanassiou, A. Reigber, and S.R. Cloude, "Vegetation and ground parameter estimation using polarimetric interferometry Part 2: Parameter inversion and optimal polarisations," Proc. ESA CEOS SAR Workshop, pp.30–33, Oct. 1999.

[12] R. Roy and T. Kailath, "ESPRIT—Estimation of signal parameters via rotational invariance techniques," IEEE Trans. Acoust., Speech & Signal Process., vol.37, no.7, pp.984–995, July 1989.

[13] S.R. Cloude and E. Pottier, "A review of target decomposition theorems in radar polarimetry," IEEE Trans. Geosci. & Remote Sensing, vol.34, no.2, pp.498–518, March 1996.

[14] S.N. Madsen, H.A. Zebker and J. Martin, "Topographic mapping using radar interferometry: Processing techniques," IEEE Trans. Geosci. & Remote Sensing, vol.31, no.1, pp.246–256, Jan. 1993.

[15] H. Akaike, "A new look at the statistical model identification," IEEE Trans. Autom. Control, vol.AC-19, no.6, pp.716–723, Dec. 1974.

[16] M. Wax and T. Kailath, "Detection of signals by information theoretic criteria," IEEE Trans. Accoust., Speech & Signal Process., vol.ASSP-33, no.2, pp.387–392, April 1985.

[17] O. Stebler, P. Pasquali, and D. Nüesch, "Investigation of multi-baseline singular value estimation within Pol-InSAR measurements," EU-SAR00 Proc., pp.257–260, 2000.

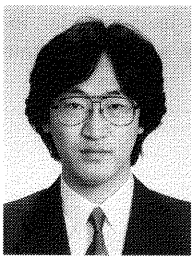

**Hiroyoshi Yamada** received the B.E., M.E., and Dr.Eng. degrees from Hokkaido University, Sapporo, Japan, in 1988, 1990 and 1993, respectively, all in electronic engineering. In 1993, he joined the Faculty of Engineering, Niigata University, where he is an associate professor. From 2000 to 2001, he was a Visiting Scientist at Jet Propulsion Laboratory, California Institute of Technology, Pasadena. His current interests involve in the field of array signal processing, radar polarimetry and interferometry, microwave remote sensing and imaging. Dr. Yamada is a member of IEEE.

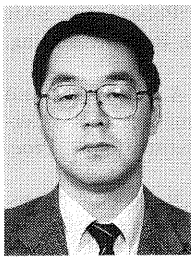

**Yoshio Yamaguchi** received the B.E. degree in electronics engineering from Niigata University in 1976, and the M.E. and Dr.Eng. degrees from Tokyo Institute Technology in 1978 and 1983, respectively. In 1978, he joined the Faculty of Engineering, Niigata University, where he is a professor. From 1988 to 1989, he was a Research Associate at the University of Illinois, Chicago. His interests are in the field of propagation characteristics of electromagnetic waves in lossy medium, radar polarimetry, microwave remote sensing and imaging. Dr. Yamaguchi is a senior member of IEEE, and a member of the Japan Society for Snow Engineering.

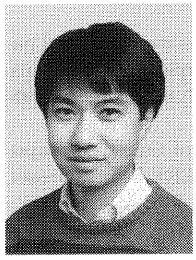

**Yunjin Kim** received the Ph.D. degree from the University of Pennsylvania in 1987. From 1987 to 1989, he was with the Department of Electrical Engineering, New Jersey Institute of Technology, as an Assistant Professor. Since 1989, he has been with the Jet Propulsion Laboratory. Currently, Dr. Kim is the radar science and engineering section manager at Jet propulsion Laboratory. He is also the Shuttle Radar Topography Mission (SRTM) project manager. He is an Associate Editor of Radio Science. His current research area includes SAR polarimetry and interferometry, SAR data calibration and processing, SAR data applications, radar system engineering, electromagnetic scattering, and advanced radar technology development. He received the NASA Exceptional Service Medal in 1995.

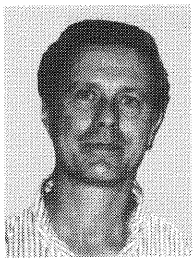

**Ernesto Rodriguez** received the Ph.D. degree in physics in 1984 from Georgia Institute of Technology, Atlanta. He has worked in the Radar Science and Engineering section at the Jet Propulsion Laboratory, California Institute of Technology, Pasadena, since 1985, where he currently leads the Radar Interferometry Phenomenology and Application group. His research interests include radar interferometry, altimetry, sounding, terrain classification, end EM scattering theory.

**Wolfgang-Martin Boerner** received his childhood education in Austral-Asia; the Abitur (B.S.) from the August von Platen Gymnasium, Mittelfranken, Germany in 1958; his Dipl. Ing. (M.S.E.E.) degree in Communications & Electromagnetic Wave Engineering from the Technische Universität München, Bavaria, Germany in 1963; and his Ph.D. degree in Electromagnetic Engineering Sciences from the Moore School of Electrical Engineering, The University of Pennsylvania, Philadelphia, PA in 1967. From 1967 to 1968 he was a Research Assistant Engineer with the EECS Radiation Laboratory of the University of Michigan, Ann Arbor, MI. In 1968 he joined the University of Manitoba at Winnipeg, Canada; since 1978 he has been a Professor at the Department of Electrical Engineering & Computer Science, the University of Illinois at Chicago, and Director of its Communications, Sensing and Navigation Laboratory. While at UIC Professor Boerner was awarded the Alexander von Humboldt Senior US Scientist, the Japan Society for the Promotion of Science Senior US Scientist and the US Navy Distinguished Senior Professor awards; and he is a University of Illinois Distinguished Senior Professor—all in recognition for his contributions to the advancements of Electromagnetic Inverse Scattering, Radar Polarimetry and Interferometry. He is a member of numerous international scientific societies; he is a senior member of the Canadian Association of Physicists (CAP), the American Society for Engineering Education (ASEE), the American and the International Societies for Remote Sensing and Photogrammetry (ASRSP &ISRSP); he is Fellow of IEEE (Institute for Electrical and Electronic Engineering), OSA (Optical Society of America), the SPIE (International Society for Applied Optics), AAAS (American Association for the Advancement of Science); he is a registered engineer with VDE (Verein Deutscher Ingenieure), APEM (Association of Professional Engineers of the Province of Manitoba), ISPE & NSPE (Illinois and US National Societies of Professional Engineers); and among others he is a member of the honor societies Sigma Xi, the American and the German Fulbright Associations, and the Alexander von Humboldt Association.